Bone mineral organization at the mesoscale: A review of mineral ellipsoids in bone and at bone interfaces

Chiara Micheletti, Ariana Hurley, Aurélien Gourrier, Anders Palmquist, Tengteng Tang, Furqan Shah, Kathryn Grandfield

This is a preprint version of the accepted manuscript
Online version: https://www.sciencedirect.com/science/article/abs/pii/S1742706122001027
doi: https://doi.org/10.1016/j.actbio.2022.02.024
Please cite as: Micheletti, C., Hurley, A., Gourrier, A., Palmquist, A., Tang, T., Shah, F.A., Grandfield, K. (2022). *Bone mineral organization at the mesoscale: A review of mineral ellipsoids in bone and at bone interfaces*, Acta Biomater. 142, 1-13. doi: 10.1016/j.actbio.2022.02.024

Bone mineral organization at the mesoscale: A review of mineral ellipsoids in bone and at bone interfaces

Chiara Micheletti[a,b], Ariana Hurley[a,c], Aurélien Gourrier[d], Anders Palmquist[b], Tengteng Tang[a,1], Furqan A. Shah[b,1], Kathryn Grandfield[a,e]*

a Department of Materials Science and Engineering, McMaster University, Hamilton L8S 4L7, ON, Canada
b Department of Biomaterials, Sahlgrenska Academy, University of Gothenburg, Gothenburg SE-413 46, Sweden
c Integrated Biomedical Engineering and Health Sciences, McMaster University, Hamilton L8S 4L7, ON, Canada
d Univ. Grenoble Alpes, CNRS, LIPhy, Grenoble F-380 0 0, France
e School of Biomedical Engineering, McMaster University, Hamilton L8S 4L7, ON, Canada
* Corresponding author: kgrandfield@mcmaster.ca
1 Equal contribution.

Abstract: Much debate still revolves around bone architecture, especially at the nano- and microscale. Bone is a remarkable material where high strength and toughness coexist thanks to an optimized composition of mineral and protein and their hierarchical organization across several distinct length scales. At the nanoscale, mineralized collagen fibrils act as building block units. Despite their key role in biological and mechanical functions, the mechanisms of collagen mineralization and the precise arrangement of the organic and inorganic constituents in the fibrils remains not fully elucidated. Advances in three-dimensional (3D) characterization of mineralized bone tissue by focused ion beam-scanning electron microscopy (FIB-SEM) revealed mineral-rich regions geometrically approximated as prolate ellipsoids, much larger than single collagen fibrils. These structures have yet to become prominently recognized, studied, or adopted into biomechanical models of bone. However, they closely resemble the circular to elliptical features previously identified by scanning transmission electron microscopy (STEM) in two-dimensions (2D). Herein, we review the presence of mineral ellipsoids in bone as observed with electron-based imaging techniques in both 2D and 3D with particular focus on different species, anatomical locations, and in proximity to natural and synthetic biomaterial interfaces. This review reveals that mineral ellipsoids are a ubiquitous structure in all the bones and bone-implant interfaces analyzed. This largely overlooked hierarchical level is expected to bring different perspectives to our understanding of bone mineralization and mechanical properties, in turn shedding light on structure-function relationships in bone.

Keywords: Bone; Biomineralization; Electron microscopy; Electron tomography; Mineral ellipsoid

1. Introduction

It is well known that a material's mechanical properties depend on its composition and structure. In the case of the material bone, said properties are influenced by the arrangement of its organic (mostly type I collagen [1,2]) and inorganic (bone apatite, a mineral rich in Ca and P [3,4]) components, together with water, across several length scales. Bone is a hierarchical material [5], [6], [7], [8], and it is this particular architecture combined with its optimal composition that makes it possible to combine high strength and toughness, a challenging compromise to achieve in conventional material design [9], [10], [11], [12]. Interest lies in understanding the nanoscopic hierarchical levels, specifically in the mineralized collagen fibrils, as they are considered the building blocks of bone [5,7]. Within each fibril, tropocollagen strands (i.e., triple helices of amino acid chains) are organized in a quarter staggered array that forms overlap and gap zones of 27 and 40 nm, respectively, resulting in an overall 67 nm-periodic banding pattern [13,14]. These collagen fibrils eventually become mineralized, but it is still unclear how such mineralization occurs [15], [16], [17], and whether it is primarily intra- or extrafibrillar [18], although evidence shows mineralization to be “crossfibrillar” in nature [19]. It is generally accepted that bone mineral consists of 50 × 25 × 3 nm3 platelets with their c-axes aligned with the collagen fibrils [20], [21], [22], [23]. Recent work has suggested that mineral platelets themselves are also a hierarchical structure, made of smaller platelets and acicular crystals, thus adding additional organization levels to the nine previously identified in lamellar bone structure [7,8] for a total of 12 levels of hierarchy at present [19].

Despite major advances in characterization techniques available to probe bone architecture [24], [25], [26], several questions still remain unanswered about bone organization at the smaller length scales, namely at the nano- and meso-/microscale. Characterization of bone at the nanoscale is often accomplished with transmission electron microscopy (TEM), especially by scanning TEM (STEM) with high-angle annular dark-field (HAADF) detectors to readily distinguish the organic and inorganic components of bone thanks to atomic number or Z-contrast imaging [27], [28], [29]. With HAADF-STEM imaging of transverse sections of mature human femoral cortical bone (i.e., bone oriented perpendicular to the long axis of the femur and majority of the osteons), Grandfield et al. identified regions of higher local mineral density, therein termed “rosettes” and defined as cross-sections of clusters of mineralized collagen fibrils around a less well-resolved central region [30]. The overall pattern created by these features resembles the “lacy motif” and “rosette motif” described by Reznikov et al., where collagen fibrils are mainly oriented oblique and orthogonal to the image plane, respectively [19].

Since these observations, characterization of mineralized bone using three-dimensional (3D) techniques with nanoscale resolution and microscale accessible volumes, namely focused ion beam-scanning electron microscopy (FIB-SEM) serial slice and view and machine learning-enabled segmentation, has elucidated the structure of these “rosettes” in 3D [31,32]. Buss et al. revealed the presence of prolate ellipsoids of mineral, termed “tesselles”, to be organized in a packed array or crossfibrillar tessellation at the mineralization front in the tibia of wildtype and mutant Hyp mice [32]. At the same time, these prolate ellipsoids of mineral were also identified by Binkley et al. in humans by examination of human femoral bone using plasma focused ion beam-scanning electron microscopy (PFIB-SEM) tomography, which revealed the presence of globular bright features that closely resemble the rosettes seen in two-dimensional (2D) HAADF-STEM images, but in a 3D volume of thousands of microns cubed. Therefore, thanks in large part to 3D imaging, these bright patches visualized in 2D STEM were now identified to be the cross-sections of 3D mineral clusters geometrically approximated by prolate ellipsoids [31]. While these studies were in mature bone, there is a long history of TEM imaging to identify the presence of mineral-rich regions organized in globular, sometimes elongated, patches at early sites of bone formation, in osteoid-rich regions and at mineralization fronts [33], [34], [35]. In 3D, Buss et al. showed mineral prolate ellipsoids evolving from mineral foci near the mineralization front [32], but how they evolve from other forms of osteogenesis remains to be thoroughly investigated and these early time-points remain largely outside of the focus of this review.

Despite a handful of papers since their discovery [31,32,36,37], and surely more to come, the mineral ellipsoid tessellated structure remains largely unrecognized and overlooked in bone literature. Yet uncovering bone architecture at this mesoscale will improve our understanding of bone's biological and mechanical functions, while informing perspectives on the causes and potential treatments for bone mineralization diseases, and strategies for designing bioinspired materials. In light of these findings, we re-examined the literature and previously acquired HAADF-STEM images and tomograms of bone from different species and/or anatomical locations and at biomaterial interfaces to seek out mineral ellipsoids that may have gone undetected in past work. This review opens with the examination of HAADF-STEM images to assess the ubiquity of mineral-rich structures across various species, anatomical locations, and biomaterials interfaces, as well as to estimate the size of these features in 2D. Second, we analyze mineral prolate ellipsoids in 3D volumes from STEM tomography, thus providing additional considerations on the morphology and dimensions of these structures. Third, we summarize the observations of mineral ellipsoids in (P)FIB-SEM tomography, which allows for a much larger volume of material to be visualized in 3D. Finally, we discuss the biomechanical implications of these structural features to highlight structure-function relationships, along with speculations about their connection with early mineralization sites.

In this review, we adopt the term “mineral prolate ellipsoids” (or simply, “mineral ellipsoids”) following the geometric terminology introduced by [31,32]. For 2D representations, we sometimes use the term “rosettes” (as named by Grandfield et al. [30]). However, many terms exist for what are likely the same structures at varying stages of mineralization, so an additional section on terminology is appended to this review.

2. 2D imaging of bone at the nanoscale: mineral ellipsoids as seen in HAADF-STEM

2.1. The rosette vs. elliptical motif

We reviewed over 150 2D HAADF-STEM images, available in the literature and from our unpublished works, in search of features analogous to the rosettes identified by Grandfield et al. in human femoral cortical bone [30] (Fig. 1A, pink outlines). In HAADF-STEM images of bone, different features are observed depending on sample orientation with respect to the collagen fibril axis. Rosettes are typically seen in the transverse plane, when the collagen fibrils are arranged perpendicularly to the image plane, i.e., viewed in cross-section or out-of-plane (Fig. 1A). Conversely, when the collagen fibrils are roughly parallel to the image plane, the characteristic collagen banding pattern is prominent (Fig. 1B, dashed white lines) and elliptical motifs span several fibrils (Fig. 1B, yellow outlines).

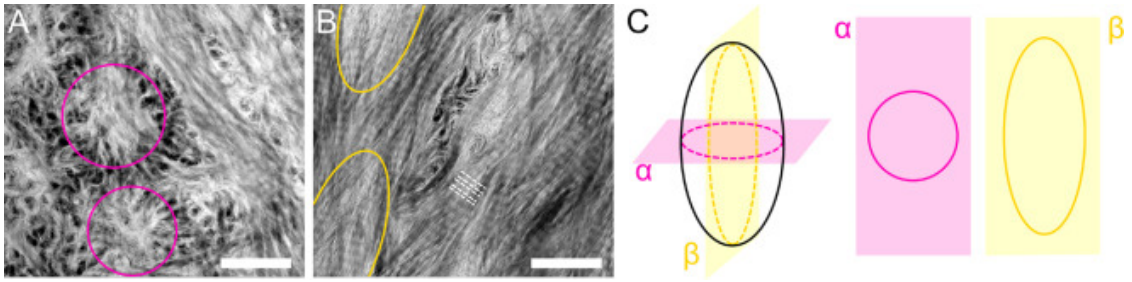

Figure 1. A, B) HAADF-STEM images of human femoral cortical bone from samples oriented perpendicularly (A) and parallel (B) to the long axis of the femur. Rosettes (pink outlines) can be identified in the perpendicular section (A), while the characteristic collagen banding is present in the longitudinal section (B, dashed white lines). Elliptical-shaped motifs (yellow outlines), as seen in B, span several collagen fibrils. C) Schematic of an ellipsoid, and its cross-sections in the orthogonal plane to the major axis (α, pink) and in the longitudinal plane along the major axis (β, yellow). This supports the theory that rosettes and elliptical motifs are cross-sectional images of the same 3D structure, i.e., a mineral ellipsoid. Scale bars are 500 nm in A and B [images A and B are adapted with permission from [30], Copyright 2018, Springer].

More specifically, these mineral ellipsoids would have a circular motif along a plane orthogonal to the major axis, and an elongated, elliptical motif in a plane perpendicular to the minor axis (Fig. 1C). Further details are provided later in the review with support from 3D imaging. The presence of these motifs in normal planes suggests they are each the cross-sections of 3D prolate ellipsoids. Mineral arranged in this elongated pattern has also been reported in the rat cranium using SEM [38] (see Section 5).

2.2. Evidence of ubiquity across species, anatomical locations, and interfaces

We analyzed HAADF-STEM images of bone from different species and/or anatomical locations to determine whether the mineral ellipsoids are also present but were unrecognized in types of bone other than human femoral cortical bone (Fig. 2A) and murine tibia [30], [31], [32]. Interestingly, we found evidence of features resembling the rosettes or elliptical motifs in bone tissue from multiple species at different anatomical locations and at interfaces with a variety of natural or synthetic materials. More specifically, typical rosettes, as marked by pink outlines, were observed in human femoral lamellar bone interfacing with hyper-mineralized tissue [39] (Fig. 2B), bone extracellular matrix (ECM) interfacing with an osteocyte lacuna [40] (Fig. 2C) and with a synthetic hydroxyapatite scaffold [41] (Fig. 2D) in human maxilla, bone ECM interfacing with an osteocyte lacuna and with a stainless steel pedicle screw coated with plasma-sprayed hydroxyapatite in human lumbar spine [42] (Fig. 2E), rat tibial bone interfacing with bioactive glass [43] (Fig. 2F), rabbit tibial bone interfacing with a titanium implant [44] (Fig. 2G), sheep cranial bone interfacing with a multi-component calcium phosphate dome implant where bone is growing outside the skeletal envelope (Shah et al., unpublished work) (Fig. 2H), and sheep and human cranial bone interfacing with an implant made of flat tiles of a multi-component calcium phosphate [45] (Fig. 2I and Fig. 2J, respectively). Not only rosettes, but also elliptical motifs, indicated by yellow arrows, were identified in some instances of bone forming at a biomaterial interface (Figs. 2C, D, E, G, H). In the majority of the samples featured, with the exception of Grandfield et al. [30] and Shah et al., unpublished work, the presence of rosettes in the HAADF-STEM images reported here has been largely ignored in the manuscripts, although the features are clearly present. This might explain the lack of information regarding the presence of the rosette structure in other types of bone tissue and their formation or orientation at bone-implant interfaces. Clearly, there is a need to collect more data from various species, anatomical locations, and interfaces with sufficient resolution and field of view to conduct a more comprehensive analysis on these mineral ellipsoids.

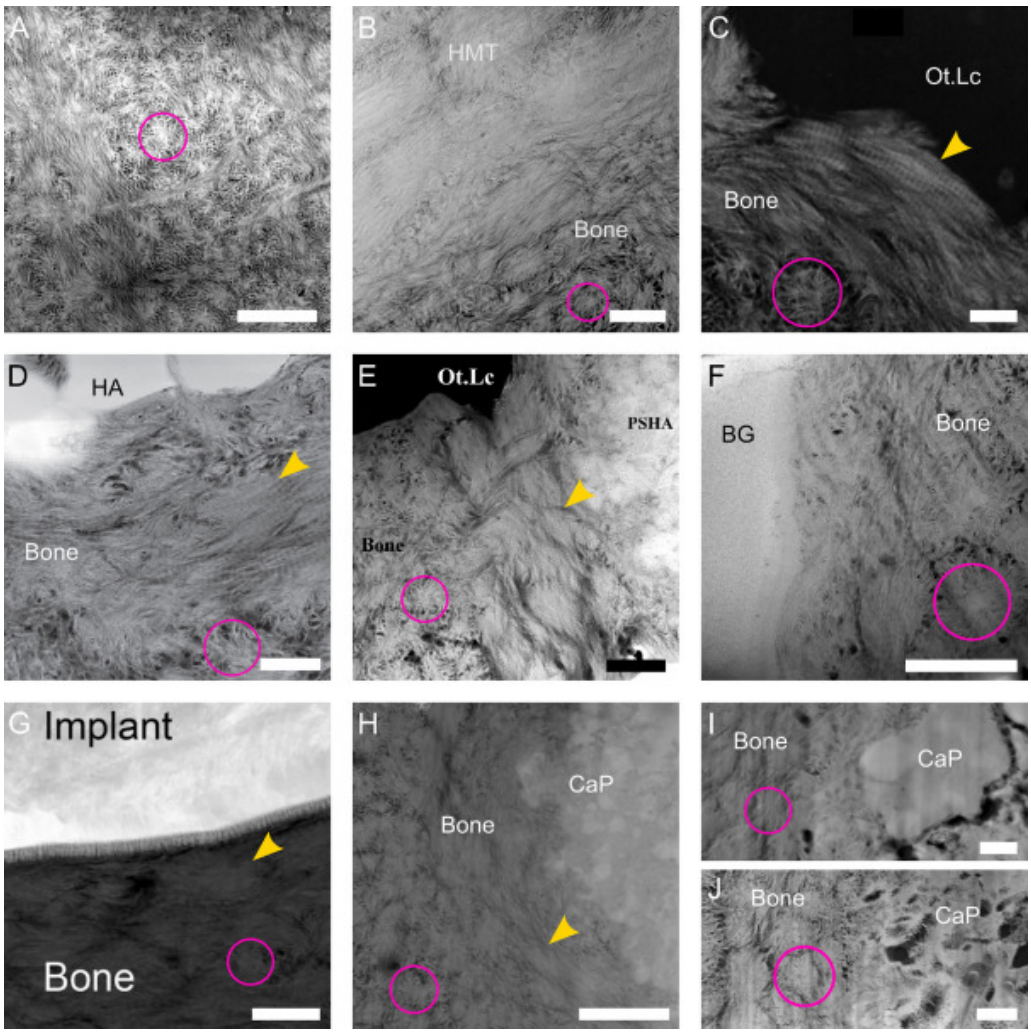

Figure 2. Representative examples of rosettes identified in HAADF-STEM images. Some rosettes in the images are outlined in pink for clarity. Bone samples correspond to: A) human femoral cortical bone, native tissue [from [30], unpublished data]; B) human femoral cortical bone, interface with a hyper-mineralized tissue (HMT) [adapted with permission from [39], Copyright 2020, Elsevier]; C) human maxilla, interface with an osteocyte lacuna (Ot.Lc) [adapted with permission from [40], Copyright 2015, American Chemical Society]; D) human maxilla, interface with a synthetic hydroxyapatite scaffold (HA) [adapted with permission from [41], Copyright 2010, Wiley Periodicals, Inc.]; E) human lumbar spine, interface with a stainless steel pedicle screw coated with plasma-sprayed hydroxyapatite (PSHA) and an osteocyte lacuna (Ot.Lc) [adapted with permission from [42], Copyright 2012, Inderscience Enterprises Ltd.]; F) rat tibia, interface with bioactive glass (BG) [from [43], unpublished data]; G) rabbit tibia, interface with a titanium implant [adapted with permission from [44], Copyright 2013, The Royal Society of Chemistry]; H) sheep cranium, interface with a multi-component calcium phosphate dome-shaped implant (CaP). In this system, bone is growing outside the skeletal envelope [Shah et al., unpublished work]; I) sheep cranium and J) human cranium, interfaces with a multi-component calcium phosphate implant in the form of flat tiles (CaP) [adapted with permission from [45], CC BY-NCsingle bondND license]. In addition to rosettes, images C, D, E, G and H also contain examples of elliptical motifs (yellow arrowheads). Uneven rosette appearance in the different images can be attributed to the variable sample preparation methods and the instrumental and imaging conditions. Scale bars are 2 µm in A and H, 1 µm in B, E F, I and J, and 500 nm in C, D and G.

2.3. Mineral ellipsoid segmentation and size measurement in 2D

Selected HAADF-STEM images of human bone were used to analyze the transverse cross-sections of mineral ellipsoids, i.e., the rosettes, semi-quantitatively in terms of size. These images included human bone from three different anatomical locations, i.e., femur, lumbar spine, and maxilla. Moreover, examples of both native bone without any interface and interfacial bone tissue (bone ECM interfacing with an osteocyte lacuna and a laser modified titanium implant [40], bone ECM interfacing with a hydroxyapatite scaffold [41], and bone ECM interfacing with an osteocyte lacuna and a hydroxyapatite-coated stainless steel screw [42]) were included in this analysis. Selection of these images was based on the clarity of the rosettes to allow for their segmentation and size measurement. A total of 83 rosette-like features were segmented, measured, and analyzed statistically. More details on the methods used for segmentation (Figure S1) and measurement are provided in Supplementary Information. Statistical analyses were carried out in Python 3.8 using the libraries "scipy.stats", "scikit_posthocs" and "statsmodel.stats". Outliers were rejected using the interquartile range (IQR) method. For comparisons between two groups only, statistical significance was determined using a Welch's t-test ($\alpha = 0.05$). For comparisons between more than two groups, statistical significance was determined using a one-way ANOVA test with Scheffe's post-hoc comparison ($\alpha = 0.05$). Normality and heteroscedasticity were verified using the Schapiro-Wilk and Levene tests, respectively ($\alpha = 0.05$). In the case of homoscedasticity violation, the one-way ANOVA test was corrected to account for unequal variances.

The diameter of the mineral ellipsoids ranged from 101 nm to 1187 nm, with an average size of 692 nm ± 196 nm (Fig. 3A). When comparing rosette size based on anatomical locations, their diameter was on average larger in human femur compared to both maxilla and spine ($p < 0.001$), while no statistically significant difference was found between maxilla and spine (Fig. 3B). However, limitations in the estimation of the rosette diameter in 2D should be noted since the image plane may intersect the 3D ellipsoids at different levels along their major axis, as can be inferred from the schematic representation in Fig. 1C which shows the alpha plane at the maximum diameter of the ellipse. It is therefore likely that these measures are an underestimation of the maximum diameter. For this reason, viewing the entirety of the ellipsoid from larger-volume 3D techniques, such as FIB-SEM tomography, provides the most accurate measures [31,32]. These results nonetheless allow for a comparison between anatomical sites and a reasonable approximation of the diameter.

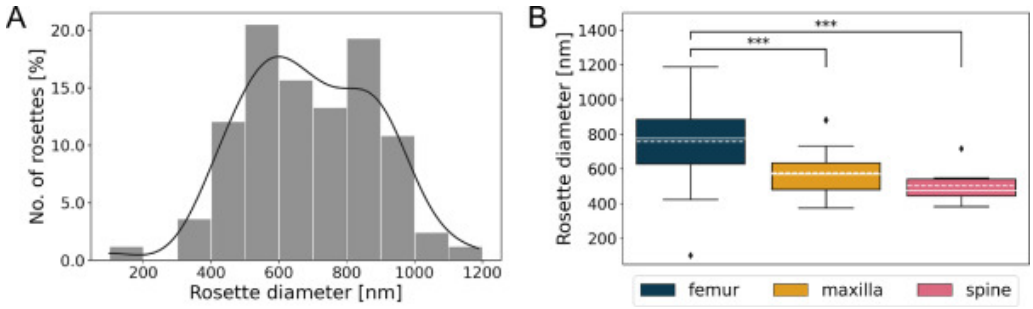

Figure 3. A) Distribution of rosette diameter (evaluated as 2D equivalent diameter). The continuous line represents the aggregate statistics in each diameter range based on the number of observations (no. of rosettes). A total of 83 rosettes were segmented and measured in human bone from different anatomical locations (femur, maxilla, spine) and with different types of interfaces. B) Box plot showing the distribution of rosette diameter based on the anatomical location, i.e., femur (blue, n = 56), maxilla (yellow, n = 19) and spine (pink, n = 8). The boxes represent 50% of the data, limited by the upper and lower quartiles, with the median and mean indicated by continuous and dashed lines, respectively, across each box. The vertical lines indicate the range of the data. Points outside of the range indicate outliers, which were excluded from statistical analyses. *** denote statistical significance ($p < 0.001$).

The same method was applied to analyze seven rosettes in rabbit bone at a titanium implant interface [44]. Their 2D equivalent diameter ranged from 455 nm to 717 nm, with an average of 618 nm ± 91 nm. No statistical difference was found in the rosette diameter between the rabbit and human bone examples ($p > 0.05$). This supports the idea that the mineral ellipsoids are ubiquitous across species and consistent in their characteristics (i.e., shape and size), suggesting that they are a distinctive structural feature in bone, analogously to the periodic banding pattern in various types of fibril-forming collagens. Nonetheless, a thorough analysis involving a larger sample size and more species is necessary for a better understanding of how mineral ellipsoids form and how they contribute to the mechanical properties of bone. In addition, there is expected to be some variation in the measurements reported here considering that it cannot be assumed that the rosettes are cut precisely at their maximum diameter, and hence their maximum cross-section is in the image plane examined.

3. 3D imaging of bone at the nanoscale: mineral ellipsoids as seen in STEM tomography

In 2D HAADF-STEM imaging, features along the thickness of the sample are projected onto the same image plane, becoming overlapped onto each other, which poses some challenges with regards to their resolution and leads to the loss of information in the third dimension [46]. In the case of bone and bone interfaces, more precise 3D analysis can be accomplished with STEM tomography [24,47] (sometimes simply referred to as "electron tomography" in this paper), in order to reconstruct a 3D volume, i.e., an electron tomogram, of the sample by acquiring a set of HAADF-STEM images of the same region at different tilt angles [48]. Three tilt series acquired as part of the work by Grandfield et al. [30] and Shah et al. [40] (unpublished electron tomograms) were examined to evaluate rosette-like features and elliptical motifs in 3D. Additional details about tilt series reconstruction, visualization and segmentation are provided in Supplementary Information. The three tomograms reconstructed from each tilt series are herein referred to as Tomogram I, Tomogram II and Tomogram III.

3.1. Tomogram I: Femoral bone transverse to its long axis

Tomogram I (Fig. 4A) depicts human femoral cortical bone with the imaging plane (xy) transverse to the long axis of the bone, and therefore to the osteons, such that the collagen fibrils are out-of-plane. Bright patches (indicated by 'i', 'ii' and 'iii' in Fig. 4A), resembling the rosette pattern observed in HAADF-STEM images, are visible in the transverse plane (xy plane) throughout the volume when viewing along the direction of the long axis of bone (z-direction) (Video S1). For clarity of visualization and to allow for size evaluation, three representative rosettes in the xy plane were segmented across the entire tomogram depth (z-direction) (Fig. 4B). From the tomogram segmentation, it appears that a rosette indeed extends in 3D, and is not simply a 2D entity. Although technical restraints related to the limited sample thickness hinder thorough characterization of the geometry and size of these mineral-rich clusters, it seems that they have a pseudo-cylindrical shape, closer to that of a prolate ellipsoid. The trend in rosette diameter (not constant, but presenting a maximum value) appears in agreement with ellipsoid-shaped solids (Figs. 4C, D). However, a larger sample volume is more suitable to investigate the overall shape and size of the mineral ellipsoids. Due to the requirement of electron transparency, samples for electron tomography are limited in size, but larger volumes could be analyzed with other techniques, such as the "serial-surface-view" in dual FIB-SEM instruments [49] (discussed more in Section 4).

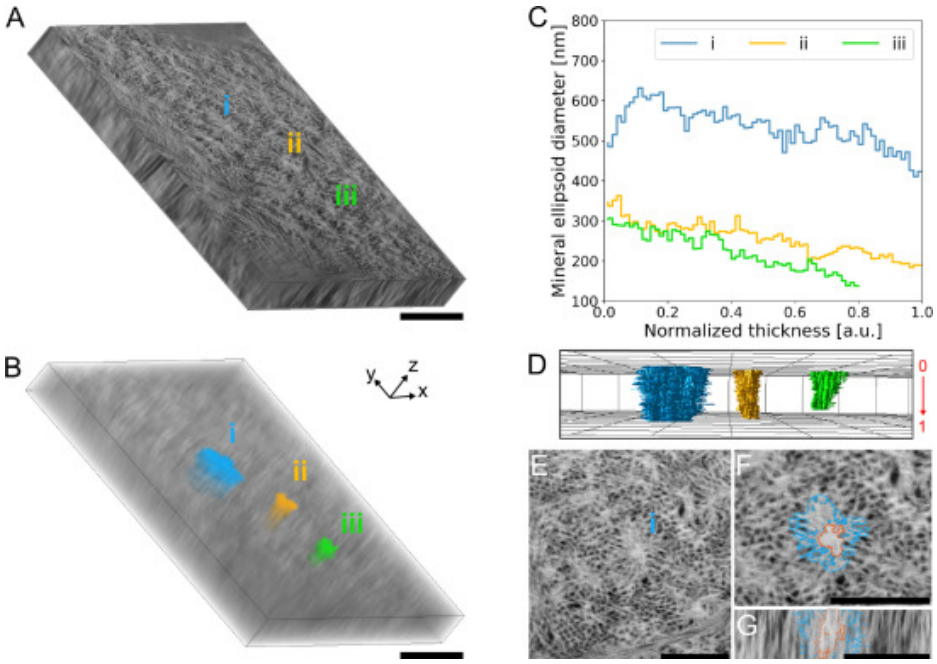

Figure 4. A) Tomogram I, corresponding to a reconstruction of an electron tomography tilt series of a section of human femoral cortical bone oriented perpendicularly to the long axis of the femur [from [30], unpublished data]. Rosette-like mineral-rich regions can be identified as the brighter, circular patches in the xy plane. B) Segmentation of three representative mineral ellipsoids (labeled as 'i', 'ii' and 'iii' in A). The volume renderings in A and B are represented as orthographic projections [note that in electron tomography, features along the z-direction are elongated due to the missing wedge of information [46]]. C) Variation in 2D equivalent diameter measured in the xy plane along the sample thickness (normalized thickness in the z-direction, corresponding to the red arrow in D) for the mineral ellipsoids 'i', 'ii' and 'iii'. The diameter variation, presenting a maximum value, supports the 3D modeling of rosettes as prolate ellipsoids. Note that 'i' and 'ii' were segmented across the entire thickness of the tomogram, while 'iii' was identified in 80% of the xy orthoslices. The ellipsoidal shape is also visible from the 3D segmentation in D [note that the 3D representation in D is not an orthographic projection, therefore no scale bar is provided]. E) mineral ellipsoids 'i' and outline of its segmentation (blue) with distinction of the mineral-rich core (orange) in representative F) xy and G) yz orthoslices. Scale bars are 1 µm.

Two of the mineral ellipsoids (labeled 'i' and 'ii') in Tomogram I were present across the entire volume thickness, while one (labeled 'iii') was segmented in 80% of the xy orthogonal slices (orthoslices) of the tomogram, as its structure appeared to merge with its surroundings making it less identifiable for segmentation purposes. The two mineral ellipsoids (labeled 'ii' and 'iii') in the proximity of the canaliculi had a maximum diameter (as measured in the xy plane) of 306 nm and 363 nm, while 'i' was at most 632 nm wide (in the xy plane), similar to the values obtained for 2D HAADF-STEM images. The smaller size of the clustering in 'ii' and 'iii' could be due to the presence of the canaliculi that poses spatial constraints, or their location further away from the ellipsoid maximum cross-section. As already observed by Grandfield et al. in 2D HAADF-STEM images [30], 3D analysis from Tomogram I also reveals that rosettes are characterized by a brighter central region, within which collagen fibrils (darker circular features) become progressively more abundant in the peripheral zone, up to the point where the rosettes appear less distinguishable when individual mineralized collagen fibrils can be observed. The fact that the rosettes and therefore the mineral ellipsoids are more mineralized in their core is indeed what makes these structures more visible among the mineralized collagen fibrils present across the entirety of the bone sample. One such example is shown in Figs. 4E, F, and G where a mineral ellipsoid (labeled 'i') has a visibly brighter core with an average diameter around 217 nm, which roughly accounts for 41% of the mean diameter of the overall ellipsoid.

As rosettes appear to be the cross-sectional image of 3D features, electron tomography seems to be a more adequate technique to investigate them compared to HAADF-STEM, where each image is a 2D projection. However, there are limitations in electron tomography that can lead to artifacts in the reconstructed tomograms, such as those arising from the missing wedge in the sampling [46]. The specific reconstruction algorithm employed can also affect the final tomogram quality, in turn influencing the understanding of the structure and morphology of the shape of mineralized ellipsoids or even cross-fibrillar mineralization. For example, using the simultaneous iterative reconstruction technique (SIRT), a different number of iterations can affect the reconstruction quality [46]. In the case of the tilt series used in Tomogram I, a higher number of iterations resulted in more grainy but less blurred orthoslices in the reconstructed tomogram, hence enabling a better rendering of the finer structures within and around an individual rosette. On the other hand, fewer iterations appear suitable to examine the overall shape and distribution of rosettes across the entire electron tomogram (see Supplementary Information).

3.2. Tomogram II: Femoral bone parallel to its long axis

In a sample oriented parallel to the long axis of a long bone, and therefore generally to the osteons, rosettes are rarely visible. Instead, the collagen appears in the plane of the image, with both the collagen banding pattern and the elliptical motifs distinguishable. For example, Tomogram II (Fig. 5A) corresponds to bone from the same human femoral cortex as Tomogram I, but prepared in the direction parallel to the long axis of bone. The characteristic banding pattern arising from the periodic arrangement of mineralized collagen fibrils is visible throughout the tomogram in the xy plane (Video S2). The organization of the fibrils also appears to define elliptical motifs (Fig. 5B, yellow outline). When viewing a cross-section of this elliptical motif along its minor axis, the observed brighter regions of higher mineral density (Fig. 5C), corresponding to a partial view of a rosette, further support that rosettes and elliptical motifs are cross-sectional views of the same 3D solid but along orthogonal planes (Fig. 1C). The analysis of electron tomograms of bone sections oriented in two orthogonal planes can provide valuable complementary information (e.g., Tomogram I and II). However, given the limited depth of the tomogram, the cross-sections of the mineral ellipsoids in Tomogram II do not fully enclose an entire rosette, therefore Tomogram I seems to be more suitable to characterize rosettes in terms of size and morphological changes across the sample thickness.

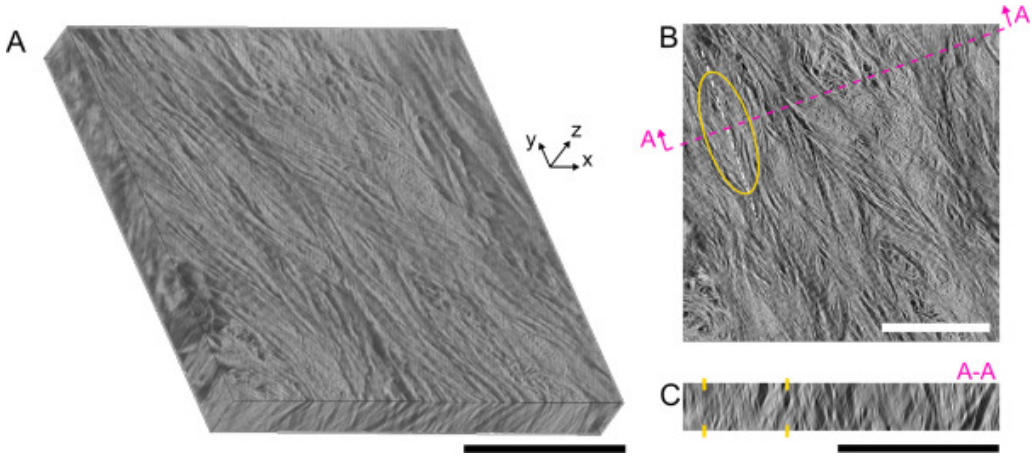

Figure 5. A) Tomogram II, corresponding to a reconstruction of an electron tomography tilt series of a section of human femoral cortical bone oriented parallel to the long axis of the femur [from [30], unpublished data]. The characteristic collagen banding pattern is visible in the tomogram, especially in the xy plane in B. Elliptical motifs span several collagen fibrils. When sectioning one of such motifs (outlined in yellow) perpendicularly to its major axis (section A-A, pink dashed line) (B), mineral-rich regions can be distinguished (C). These could correspond to rosettes, but the sample thickness is too limited to confirm it. The volume rendering in A is represented as an orthographic projection [note that in electron tomography, features along the z-direction are elongated due to the missing wedge of information [46]]. Scale bars are 1 µm.

3.3. Tomogram III: Maxillary bone at the bone–osteocyte lacuna interface

Tomogram III (Fig. 6A) is the reconstructed volume of a bone ECM-osteocyte interface in the vicinity of a titanium implant (not visible in Tomogram III) placed in the human maxilla. The mineralized collagen fibrils tended to appear more disorganized in the xy plane compared to Tomogram I and Tomogram II. This may be attributed to the fact that the sample was prepared without specific consideration for the dominant loading axis of the implant in the maxilla during mastication. Closer to the osteocyte lacuna, the collagen banding pattern is more visible (Fig. 6B, arrowhead), which also results in some elliptical motifs being observable. Further away from the cell lacuna, the fibrils appear to orient in the direction perpendicular to the xy plane, and some brighter patches, resembling rosettes, can be distinguished (Fig. 6B) and their extension in 3D can be confirmed by looking at the reconstruction (Video S3). Rosettes present in the xy plane in Tomogram III are less defined than those in Tomogram I, which could depend on the different bone type and/or the presence of an interface, as well as sample-specific characteristics (such as orientation), and eventual artifacts in the sample preparation and/or data acquisition. However, as rosettes and elliptical motifs were observed across the different samples, it is highly likely that the mineral ellipsoids are to be found in bone tissue independently of the anatomical location and the presence of an interface.

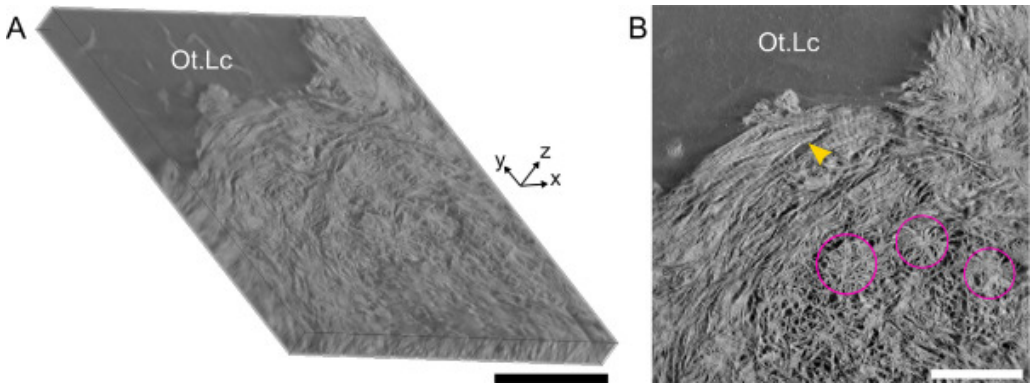

Figure 6. A) Tomogram III, corresponding to a reconstruction of an electron tomography tilt series of human maxilla ECM at the interface with an osteocyte lacuna (Ot.Lc) [from [40], *unpublished data*]. B) Representative xy orthoslice of Tomogram III. In the proximity of the osteocyte lacuna, collagen banding pattern and elliptical motifs are visible (yellow arrowhead). Further away, bright patches corresponding to rosettes are present (pink outlines). The volume rendering in A is represented as an orthographic projection [note that in electron tomography, features along the z-direction are elongated due to the missing wedge of information [46]]. Scale bars are 1 µm.

4. 2D and 3D imaging of bone at larger fields of view: mineral ellipsoids as seen in SEM and (P)FIB-SEM

HAADF-STEM allows us to obtain high resolution images of bone features at the nano- and mesoscale. By adding a third imaging dimension in STEM tomography, more information pertaining to the mineral structure can be gathered. While STEM offers a very high resolution (subnanometer), samples need to be extremely small and thin, in particular electron transparent, typically ~100–200 nm thick. This makes the volume analyzed in electron tomograms limited in size (at most ~1 µm3) [49,50], which can restrict the understanding of structural features that extend beyond the nanoscale and into the meso-/microscale, such as the mineral ellipsoids we describe herein. Acquisition of SEM images in a serial slice and view fashion in FIB-SEM tomography can generate 3D tomograms of bone structure with submicron/nanometer resolution and a volume much bigger than in electron tomography [49], [50], [51], thus allowing for a more global understanding of the mineral ellipsoids.

By imaging a significantly large volume (28.6 × 25.6 × 8.7 μm3) of a human femoral cortical bone sample with a PFIB dual beam instrument, Binkley et al. observed the presence of circular, bright features across the entire tomogram in the plane transverse to the long axis of bone [31]. In work published at the same time, Buss et al. reported analogous features in the tibia of wildtype and mutant Hyp mice using FIB-SEM tomography [32]. As imaging contrast in backscattered electron (BSE)-SEM images arises from compositional differences [52,53], similarly to the Z-contrast in HAADF-STEM, these bright regions correspond to areas of higher mineral content in bone tissue. This, combined with the comparable shape and size of rosettes in HAADF-STEM images, led to the conclusion that they are indeed the same feature, offering a linkage to the nanoscale [31] (Fig. 7A). When analyzing these structures in 3D, Binkley et al. were able to identify ellipsoids approximately 700 nm wide and 1 μm long [31] (Fig. 7B). The diameter of these ellipsoids is comparable to the 2D equivalent diameter of the rosettes we analyzed in HAADF-STEM images and also close to the diameter of the mineral ellipsoid 'i' segmented in Tomogram I. In the wildtype and Hyp mice, the packing of prolate ellipsoids with a median size of around 900 nm was postulated to result in a crossfibrillar mineral tessellation pattern, which lacks continuity in the Hyp mouse [32] (Fig. 7C). Interestingly, features with a similar shape and size as the mineral prolate ellipsoids have also been observed in demineralized samples in prior work. For example, Reznikov et al. revealed the presence of "hour-glass shapes" in demineralized human lamellar bone, originating from a differential staining of aligned collagen fibrils [8]. Cross-sections of mineral ellipsoids from human femoral cortical bone samples in three orthogonal planes [31] (Fig. 7D) appear to resemble a highly contrasting circular region of material observed in a demineralized sample from the alveolar bone of a minipig [54] (Fig. 7E). The staining heterogeneities observed in demineralized bone, that result in high contrast regions like the hour-glass profiles [8], are believed to arise from non-collagenous organics (presumably proteoglycans) [8,54]. This appears analogous to the "crystal ghosts", i.e., regions rich in non-collagenous protein remainders of early calcification sites upon demineralization [55,56]. Other studies have shown the bone phosphoprotein "osteopontin" in close association with electron dense patches in demineralized chicken bone [57] and at early mineralization sites in the osteoid [58]. If the bright regions in demineralized bone samples are what is left of mineral ellipsoids upon demineralization, this could indicate that the distribution of the collagenous and non-collagenous organic components in bone is related to the organization of the mineral in the ellipsoids. However, it cannot be totally excluded that the most sheltered mineral cannot be fully removed upon demineralization, and hence contributes to image contrast in those dense regions observed in demineralized samples by FIB-SEM.

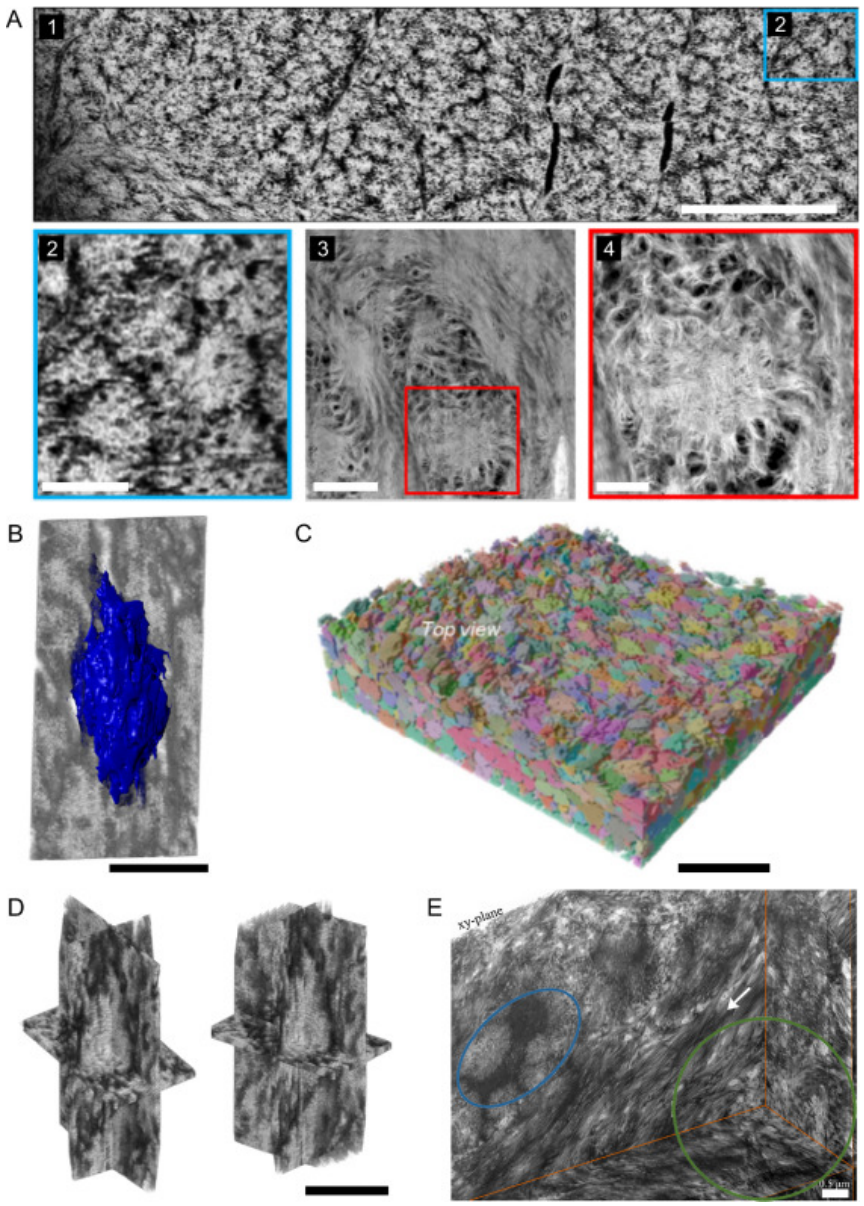

Figure 7. A) Brighter patches as observed in BSE-SEM images from PFIB-SEM tomography (images 1 and 2) and in HAADF-STEM images (images 3 and 4). Based on how the contrast is generated in both techniques, these regions indicate areas with more mineral present. This sequence of images represents the linkage between nanoscale and mesoscale, i.e., rosettes visualized in HAADF-STEM (images 3 and 4) and mineral ellipsoids identified in PFIB-SEM (images 1 and 2). B) Segmented mineral ellipsoid identified in a PFIB-SEM tomogram of a bone sample from human femoral cortex. The prolate ellipsoid is roughly 700 nm wide and 1 µm long. C) Segmentation and labeling (colouring) of abutting mineral prolate ellipsoids in a FIB-SEM tomogram of a bone sample from the tibia of a wildtype mouse. D, E) Analogous bright patches observed at the intersection of three orthogonal planes in (P)FIB-SEM tomograms. Image D corresponds to a mineralized sample, hence the brighter region is more concentrated in mineral. On the other hand, sample in E is demineralized and stained, thus the brighter area circled in green has more organic phase present. Considering the similarity in shape and size, this may indicate that these features correspond to the same structure, thus suggesting that mineral ellipsoids have a higher concentration of both inorganic and organic components. Scale bars in panel A are 5 µm in image 1, 1 µm in image 2, 500 nm in image 3, and 200 nm in image 4. Scale bars are in 1 µm in B and D, 5 µm in C and 0.5 µm in E [images A, B and D are adapted with permission from [31], Copyright 2020, Elsevier; image C is adapted with permission from [32], Copyright 2020, Elsevier; image E is adapted with permission from [54], Copyright 2019, Elsevier].

Mineral ellipsoids are overall more apparent in (P)FIB-SEM tomograms compared to electron tomograms. This can be attributed to the lower resolution of (P)FIB-SEM imaging [59], which enables the visibility of the global contour of a mineral ellipsoid rather than the finer details composing its structure and the spaces in between different ellipsoids. (P)FIB-SEM tomography and electron tomography should be used in a complementary fashion: the former to examine larger volumes of material [49], [50], [51], hence assessing global properties of the mineral ellipsoids; the latter to achieve a higher resolution [59], thus characterizing each individual mineral ellipsoid and resolving its finer details and surroundings.

5. Biomineralization and structure-function relationships

While the mesoscale description of mineral prolate ellipsoids in fully mineralized bone tissue is fairly recent [31,32], mineral-rich formations in bone have been identified before, often in association with early stages of tissue mineralization and where mineralization is ongoing. Although the process of biomineralization is still not fully understood [15], [16], [17], many electron microscopy studies have shown that the areas where mineralization begins consist of roundish aggregates of crystals (mineralization nodules) [55]. Bernard and Pease observed spherulitic mineral formations, termed “bone nodules”, ranging from 150 nm to 750 nm in size, originating from coalescing calcification sites in the osteoid from the calvariae of fetal mice [33] (Fig. 8A). The presence of roundish or elongated clusters of crystals developing during the mineralization process was also assessed by Bonucci [56]. Both studies concluded that these structures are highly concentrated in both mineral and organic substances, postulated to be polysaccharides [33] or non-collagenous proteic filaments [56], as apparent when analyzing decalcified tissues. Around the same time, Boyde and Hobdell reported the presence of clusters of mineral particles around 300 nm in diameter in the mineralization front at the periosteal surfaces of primary membrane bone [60]. In addition to these ex vivo examinations, mineral-rich structures have also been found in vitro in cultures of MC3T3-E1 (murine calvaria-derived pre-osteoblastic cell line) [61]. These “mineralization foci” appear as 100 nm globules within the collagen matrix, and progressively merge to form larger mineral aggregates [61]. Other in vitro studies have discussed the presence of calcium phosphate aggregates transported to the ECM by vesicles expelled from osteoblasts [62]. Fine mineral structures progressively start protruding from these aggregates as mineralization proceeds (Fig. 8B). Such mineral structures, that appear to connect different collagen fibrils, resemble the mineral platelets ‘bridging’ distinct rosettes in the images and tomograms we examined, i.e., recalling crossfibrillar mineralization as identified by Reznikov et al. [19]. However, caution should be exerted when comparing in vitro and in vivo/ex vivo findings.

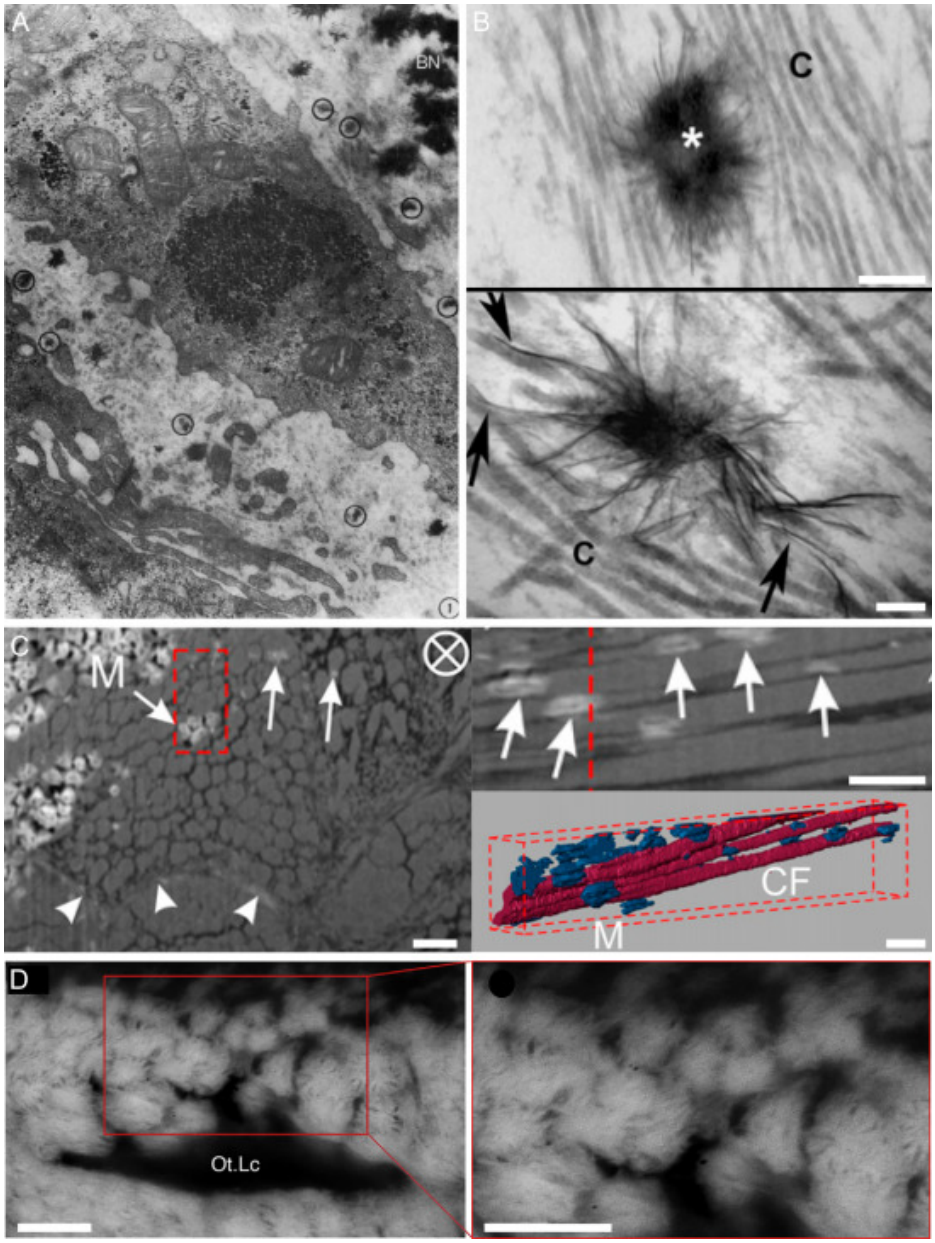

Figure 8. Examples of mineral deposits in not fully mineralized bone tissue: A) initial calcification sites (circles) and bone nodules (BN) in the calvariae of fetal mice (TEM image, magnification is x38,000 in the original paper) [adapted with permission from [33], Copyright 1969, Wiley-Liss, Inc.]; B) calcium phosphate aggregate (marked by *) associated with collagen fibrils (C label in the images) in the ECM (top image) and mineral (arrows) protruding from a mineral aggregate (bottom image) [adapted with permission from [62], National Academy of Sciences]; C) FIB-SEM images (left and top right images) and 3D reconstruction (bottom right image) of mineral deposits (M label and arrows in the images, blue in the reconstruction) at the interface between mineralized and unmineralized regions in the turkey tendon [adapted with permission from [35], PNAS license]; D) cross-sectional views of marquise-shaped motifs in the roof over an osteoblastic-osteocyte lacuna (Ot.Lc) in the rat cranium (BSE-SEM image) [adapted with permission from [38], CC BY license]. Scale bars are 0.2 μm in B, 1 μm in C and 2 μm in D.

Not only are mineral structures present (and detectable) at early stages of mineralization, but they have also been identified at the interface between poorly and completely mineralized tissue. Calcified, spherical or fusiform bodies, sometimes referred to as “calcospherulites” or “calcospherites” have been reported by several studies [34,[63], [64], [65], [66], [67]. Calcospherulites, a similar nodule-like mineralized cluster, have also been recognized as a characteristic feature of rapid bone formation in woven bone [68,69], although it remains unknown if the prolate ellipsoids reviewed herein arise directly from calcospherulites since bone remodeling may presumably change them as bone matures. Mineral deposits with a prolate ellipsoidal shape have been observed in turkey tendons along the long axis of the tendon, both around and within collagen fibrils [35] (Fig. 8C). Mineralization foci have also been reported at the transition between osteoid and mineralized tissue in human osteons [70]. In addition, micron-sized mineral globules seem to be a characteristic feature at the mineralization front of a hyper-mineralized layer of bone tissue in the human femoral neck that often manifests with aging [39]. Near the mineralization front in the tibial diaphysis of a wildtype mouse, mineral foci appear to grow into packed prolate ellipsoids, a phenomenon that is also present but in a defective way in a mutant Hyp mouse affected by X-linked hypophosphatemia [32].

The neurocranium is an ideal location to study the development of bone structure, due to continuous bone growth at the cranial sutures [71,72]. Examining deproteinized bone at the apex of the finger-like projections at the suture edge, Shah et al. assessed the evolution of bone mineral morphology from discrete “marquise-shaped motifs” into a continuous interwoven mesh [38]. A parallel can be drawn between the marquise-shaped motifs at the cranial bone-suture interface [38] and the mineral ellipsoids in femoral cortical bone [31], based on their comparable shape and size. Moreover, marquise-shaped motifs viewed in cross-section using BSE-SEM appear to be circular clusters of mineral platelets [38] (Fig. 8D), and closely resemble the rosettes in HAADF-STEM images and the cross-sections of mineral ellipsoids in PFIB-SEM tomograms [31].

In addition to unclear aspects concerning osteoid mineralization, different models have been proposed concerning the relative location of mineral and collagen once biomineralization is complete (in a relative sense, as bone remodeling and hence mineralization are ever occurring phenomena throughout the entire life of the tissue). Early electron microscopy investigations placed the mineral mainly within the gap zone of the staggered tropocollagen molecules (intrafibrillar mineralization), eventually extending in the overlap region [73], [74], [75], [76]. On the other hand, other work proposed that most mineral is located outside the collagen fibrils (extrafibrillar mineralization) [77,78], in the form of platelets wrapped around the fibrils [79], [80], [81]. In between these two opposite views, more recent studies support the idea that mineral is neither exclusively intra- or inter-/extrafibrillar, but crossfibrillar [19]. This correlates to what was observed for osteoid mineralization, as mineral foci have been identified both within and outside a single fibril [35]. Observation of mineral ellipsoids in human femoral cortical bone [31] and mouse tibia [32] and their “crossfibrillar tessellation” [32] further supports that the mineral-collagen relation spans across several fibrils, and it is not organized in a mere intra- or interfibrillar fashion, consistently with the hierarchical organization of bone given by Reznikov et al. [19]. Tessellated prolate ellipsoids of mineral, which have also been termed “tesselles” [32,36,37], appear to develop from nanosized mineral foci, that progressively enlarge to grow inside collagen bundles [32].

The implications of collagen mineralization and bone hierarchical organization are not purely biological: a better understanding of the collagen-mineral architecture is important not only to shed light on biology-related aspects such as bone pathologies, but also from an engineering and materials science perspective [82]. Like in any other material, bone's structure and properties are deeply interrelated. Bone is a noteworthy material, as it is both strong and tough, a compromise often hard to achieve in man-made materials [10]. These unique properties are partially a result of the multiscale hierarchical architecture of bone [5,6,9,11,12]. Exhaustive knowledge of bone structure would be of interest in the development of bioinspired materials, both in the implantable biomaterials and tissue engineering fields [83], and beyond biomedical applications [84,85]. Collagen mineralization, whether it is intra-, inter-/extra-, or crossfibrillar, influences the final mechanical properties of bone, as the type of mineralization ultimately dictates the spatial arrangement of the constituents of the composite material bone, i.e., collagen and mineral. In fact, the mechanical behavior of composite materials, for a given composition, depends on the size and distribution of their constituents.

Therefore, the mineral ellipsoids at the mesoscale level in bone architecture would have obvious mechanical implications. Specifically, the dense packing of mineral ellipsoids has been proposed to originate a tessellated structure, which offers resistance to bending and compression at the tesselles interface [32]. Tessellation of subunits packed with chemically or physically distinct interfaces is common in natural materials to combine stiffness and strength with toughness by reducing crack propagation [86]. Examples of tessellation are found in several invertebrates and vertebrates [86], in both the exoskeleton (e.g., armored fish scales [87,88] and turtle shell [89,90]) and the endoskeleton (e.g., cartilage of sharks, rays and chimaeras [91,92]), as well as in the osteoderm (e.g., armadillo armor [93]) and in teeth (e.g., teeth of durophagous stingrays [94]). An example of a tessellated-like structure, where abutting elements provide mechanical interlocking at large deformations, can also be found in the human skull [11].

6. On the nature of mineral clustering: temporal evolution and technique-dependent visualization

For a deeper understanding of bone hierarchical structure and its functional and mechanical implications, extensive characterization of the clustering of mineral into ellipsoids is necessary. Specifically, the relationship between early calcification sites and mineral ellipsoids should be thoroughly investigated. We speculate such relationship to be temporal in nature, where the globular/elongated mineral aggregates observed at early mineralization stages would act as precursors and growth templates for the mineral ellipsoids. Recent work shows how mineral foci at the mineralization front progressively develop into packed prolate ellipsoids in the mouse tibia [32]. Our review highlights the ubiquitous presence of 2D rosettes and 3D ellipsoids even in areas not in proximity of a mineralization front or of osteoid-rich regions. More studies are needed to understand whether such mineral ellipsoids present in fully mineralized tissue also correspond to the evolution of early calcification sites. This would indicate that their prolate ellipsoid structure as observed nearby a mineralization front is maintained once mineralization is complete. The shape preservation and the lack of fusion of the mineral ellipsoids in mature bone could be dictated by the action of mineralization inhibitors [95]. The hypothesis of a correspondence between calcification sites and mineral prolate ellipsoids is favoured by similarities in shape and size, in addition to the evolution observed at a mineralization front [32]. Studies have shown that early mineralization foci are rich in organic material, especially non-collagenous proteins such as osteopontin [58]. The presence of hour-glass/globular regions highly concentrated in organic substances has also been observed in mature demineralized bone [8,54], as previously discussed in Section 4. If these regions are what is left of decalcified mineral ellipsoids, this would be another analogy between mineral prolate ellipsoids and mineralization foci.

While bright patches indicating mineral-rich areas are clearly visible throughout the entirety of the sample in (P)FIB-SEM tomography [31,32], these structures are still identifiable but less omnipresent in HAADF-STEM images and electron tomograms (Sections 2 and 3). STEM requires the use of small and extremely thin samples, thus it is likely that only a small number of mineral ellipsoids are present within a sample so that they are cross-sectioned along a plane containing their minor axis and normal to their major axis. It is also possible that cross-sections of mineral ellipsoids (i.e., rosettes) are overall more apparent in techniques with lower resolution, as inner features, edges and mineral structures connecting different clusters of mineral are not well resolved, hence neighbouring rosettes may be seen as one. The effect of image resolution and post-processing techniques on the mineral ellipsoids characterization is evident in our comparison between Tomogram I and Tomogram I100 (see Supplementary Information), where a different blur level in the reconstruction makes the clarity of the overall mineral shape prevail over that of the finer details in Tomogram I, and vice versa for Tomogram I100 (Figure S2). In (P)FIB-SEM, a tomogram is a stack of 2D images, originated from BSE signal in the case of mineral ellipsoids studies. Given the nature of BSE imaging in (P)FIB-SEM, each image is made of signal produced in a certain region below the surface (whose depth depends on the elements involved) [52,53].

This could result in artifacts of the real morphology of the mineral ellipsoids, as what appears in an image is the average signal from a certain region, which can make mineral-rich areas located just underneath the sample surface mask those mainly composed of collagen and other organic substances. Similar issues may arise in HAADF-STEM images. As these images represent a 2D projection of the sample volume, larger mineral formations could hide the smaller ones and the organic-rich areas located along the same vertical in the sample thickness. This issue can be solved by 3D reconstructions with electron tomography.

Finally, it must be noted that the visualization of certain features in bone samples also depends on how well these structures are preserved during the preparation of ultrathin section for (S)TEM analysis. In this review, we focused on samples prepared by FIB dual beam instruments. The in situ lift-out protocol applied in these instruments can maintain high integrity in bone and bone interfaces, introducing less damage and structural disruption than other techniques such as ultramicrotomy [96], [97], [98].

7. A final terminology remark

The terms “mineral prolate ellipsoid” [31,32] and “tesselle” [32] were introduced when reporting on these features in the structure of bone at the mesoscale. “Prolate ellipsoid” is a clear reference to the geometrical shape that best approximates these mineral regions, while the French term “tesselle” was coined by Buss et al. to refer to their role as components of the 3D tessellated pattern they produce [32]. One might instead consider the terms “tessella” (plural “tessellae”) or “tessera” (plural “tesserae”) which are generally defined as tiles used in tessellated patterns, albeit for 2D arrangements or tiling. However, since the term "tesserae" has been used for many years to describe the several micron-sized features within the skeletons of sharks and rays [86,99], perhaps "tessella" and "tessellae", which indicate a diminutive size, are the more appropriate English terms to describe these mineral features as tiles of a tessellated structure. Since their packing dictates further investigation, we prefer to refer to them as mineral ellipsoids in this manuscript, or slight variations such as mineral prolate ellipsoids. We also adopt the term “rosette” to indicate the 2D transverse cross-section of a mineral ellipsoid, as identifiable in HAADF-STEM images or in individual planes of PFIB-SEM volumes and electron tomograms. The term “rosette” was borrowed from work previously published by our group [30], but it must not be confused with what Reznikov et al. call “rosette”, i.e., one of the motifs present in lamellar bone [19]. In that work, the overall pattern created by what we call rosettes more closely resembles what is indicated as “lacy motif” instead [19]. When referring to mineral formations identifiable at the early stages of mineralization, the term “mineralization foci” or “mineral foci” is used by several authors [32,58,61,70]. Others instead label these early mineralization sites as “calcospherulites”, “calcospherites” and such [34,[63], [64], [65], [66], [67] (see the terminology note in [34]). The term “bone nodules” has also been adopted by some early studies [33]. Similarly shaped and sized structures in demineralized bone have been referred to as “crystal ghosts” [55,56] or “hour-glass shapes” [8] which presumably represent the same structures. Finally, describing mineral ellipsoids as clusters of mineral should not be confused with Posner's clusters, which refer to the nanosized aggregate precursor of amorphous calcium phosphate [100].

As confusion may arise from inconsistent terminology, efforts must be made to unify the jargon. However, the use of different terms used to indicate mineral ellipsoids in fully mineralized bone tissue with respect to mineral-rich structures in the osteoid and at the mineralization front (mineralization foci) could be justified to better emphasize the different stages of mineralization.

8. Conclusion

We thoroughly reviewed the presence of mineral prolate ellipsoids in various types of bone tissues and at bone interfaces. Our collection of HAADF-STEM images shows mineral ellipsoids in 2D (as rosettes) in different species and/or anatomical locations, as well as at several types of interfaces (both natural and synthetic), thus suggesting that these features are ubiquitous in bone.

Rosettes displayed an average diameter of roughly 700 nm, in agreement with the dimension along the minor axis of the mineral ellipsoids shown in (P)FIB-SEM tomograms [31,32], as well as the size of mineral-rich structures reported at early mineralization sites [33], [34], [35]. Our segmentation of electron tomograms substantiates the view that rosette and elliptical motifs are mutually orthogonal, cross-sectional planes of mineral prolate ellipsoids, as concluded from previous (P)FIB-SEM tomography [31,32]. Considering the implications on biomineralization and mechanical properties that mineral tessellations have, these features should be extensively studied further. Comprehensive characterization should be aided by different techniques to gather complementary information across multiple length scales. At the nanoscale, the arrangement of organic and inorganic components within an individual mineral ellipsoid should be investigated. At successive levels of organization, the overall morphology and arrangement of mineral ellipsoids with respect to each other should be assessed, specifically to further explore the crossfibrillar tessellation model [32]. In addition, considering the evidence of the ubiquity of mineral clustering into ellipsoids across different species and bone types herein presented, research on mineral ellipsoids should involve bone tissue from a diverse range of animals and anatomical locations, as well as variable tissue age, and at implant interfaces. Finally, the origin and evolution of such mineral ellipsoids should be further examined, in particular to assess whether similarly shaped and sized mineral-rich structures often observed at the early stages of mineralization indeed represent a precursor state of mineral ellipsoids in all mature tissue and various forms of osteogenesis.

Declaration of Competing Interest

The authors declare that they have no known competing financial interests or personal relationships that could have appeared to influence the work reported in this paper.

Acknowledgements

We thank our collaborators who contributed some of the images reported in this work. We would also like to express our gratitude to the reviewers who provided us with valuable feedback, making it possible to enrich the quality of this review. C.M. is thankful to Mitacs (Globalink Research Award) and to the Foundation Blanceflor. Financial support from the Swedish Research Council (grant no. 2020–04715), the Swedish Foundation for International Cooperation in Research and Higher Education (grant no. STINT IB2019–8243), the IngaBritt and Arne Lundberg Foundation, the Hjalmar Svensson Foundation, the Kungliga Vetenskaps- och Vitterhets-Samhället i Göteborg, and the Doktor Felix Neubergh Foundation is acknowledged. A.G. and K.G. acknowledge frunding from the Human Frontier Science Program (grant no. RGP0023/2021). K.G. also acknowledges the Natural Sciences and Engineering Research Council of Canada (NSERC) (grant no. RGPIN-2020–05722), the Ontario Ministry of Research, Science, and Innovation (Early Researcher Award ER17–13–081), and the Canada Research Chairs Program from whom K.G. holds the Tier II Chair in Microscopy of Biomaterials and Biointerfaces.

References

[1] J.A. Buckwalter , M.J. Glimcher , R.R. Cooper , R. Recker , Bone Biology - Part I: structure, blood supply, cells, matrix and mineralization, J. Bone Joint Surg. Am. 77 (1995) 1256–1275 .

[2] J.D. Currey , Collagen and the mechanical properties of bone and calcified cartilage, in: P. Fratzl (Ed.), Collagen, Springer, Boston, MA, 2008, pp. 397–420 .

[3] W.E. Brown , L.C. Chow , Chemical Properties of Bone Mineral, Annu. Rev. Mater. Sci. 6 (1976) 213–236 .

[4] C. Rey , C. Combes , C. Drouet , M.J. Glimcher , Bone mineral: update on chemical composition and structure, Osteoporosis Int 20 (2009) 1013–1021 .

[5] S. Weiner , H.D. Wagner , The material bone: structure-Mechanical Function Relations, Annu. Rev. Mater. Sci. 28 (1998) 271–298 .

[6] P. Fratzl , R. Weinkamer , Nature's hierarchical materials, Progr. Mater. Sci. 52 (2007) 1263–1334 .

[7] N. Reznikov , R. Shahar , S. Weiner , Bone hierarchical structure in three dimensions, Acta Biomater. 10 (2014) 3815–3826 .

[8] N. Reznikov , R. Shahar , S. Weiner , Three-dimensional structure of human lamellar bone: the presence of two different materials and new insights into the hierarchical organization, Bone 59 (2014) 93–104 .

[9] R.O. Ritchie , M.J. Buehler , P. Hansma , Plasticity and toughness in bone, Phys. Today 62 (2009) 41–47 .

[10] R.O. Ritchie , The conflicts between strength and toughness, Nat. Mater. 10 (2011) 817–822 .

[11] R. Weinkamer , P. Fratzl , Solving conflicting functional requirements by hierarchical structuring—Examples from biological materials, MRS Bull. 41 (2016) 667–671 .

[12] J.D. Currey , Bones: Structure and Mechanics, Princeton University Press, Princeton NJ, 2002 .

[13] A .J. Hodge , J.A . Petruska , Recent studies with the electron microscope on ordered aggregates of the tropocollagen macromolecule, in: G.N. Ramachandran (Ed.), Aspects of Protein Structure, Academic Press, New York, 1963, pp. 289–300 .

[14] J.A . Petruska , A .J. Hodge , A subunit model for the tropocollagen macromolecule, PNAS 51 (1964) 871–876 .

[15] A.L. Boskey , Biomineralization: conflicts, challenges, and opportunities, J. Cell. Biochem. 72 (1998) 83–91 .

[16] F. Nudelman , A.J. Lausch , N.A.J.M. Sommerdijk , E.D. Sone , In vitro models of collagen biomineralization, J. Struct. Biol. 183 (2013) 258–269 .

[17] L. Addadi , S. Weiner , Biomineralization: mineral formation by organisms, Phys. Scripta 89 (2014) 098003 .

[18] H.P. Schwarcz , D.M. Binkley , L. Luo , K. Grandfield , A search for apatite crystals in the gap zone of collagen fibrils in bone using dark-field illumination, Bone 135 (2020) 115304 .

[19] N. Reznikov , M. Bilton , L. Lari , M.M. Stevens , R. Kröger , Fractal-like hierarchical organization of bone begins at the nanoscale, Science 360 (2018)

[20] P. Fratzl , S. Schreiber , K. Klaushofer , Bone mineralization as studied by small--angle X-ray scattering, Connect. Tissue Res. 34 (1996) 247–254 .

[21] J.-.Y. Rho , L. Kuhn-Spearing , P. Zioupos , Mechanical properties and the hierarchical structure of bone, Med. Eng. Phys. 20 (1998) 92–102 .

[22] H.-.R. Wenk , F. Heidelbach , Crystal alignment of carbonated apatite in bone and calcified tendon: results from quantitative texture analysis, Bone 24 (1999) 361–369 .

[23] S. Weiner , W. Traub , Crystal Size and Organization in Bone, Connect. Tissue Res. 21 (2009) 259–265 .

[24] K. Grandfield , Bone, implants, and their interfaces, Phys. Today 68 (2015) 40–45 .

[25] M. Georgiadis , R. Müller , P. Schneider , Techniques to assess bone ultrastructure organization: orientation and arrangement of mineralized collagen fibrils, J. R. Soc. Interface 13 (2016) 20160088 .

[26] D.M. Binkley , K. Grandfield , Advances in Multiscale Characterization Techniques of Bone and Biomaterials Interfaces, Acs Biomater. Sci. Eng. 4 (2017) 3678–3690 .

[27] Imaging in STEM, in: C.B. Carter, D.B. Williams (Eds.)Transmission Electron Microscopy. Diffraction, Imaging and Spectrometry, Springer, New York NY, 2016 .

[28] S.J. Pennycook , Structure determination through Z-contrast microscopy, Adv. Imag. Electr. Phys. 123 (2002) 173–206 .

[29] S.J. Pennycook, P.D. Nellist (Eds.), Scanning Transmission Electron Microscopy. Imaging and Analysis, Springer, New York NY, 2011 .

[30] K. Grandfield , V. Vuong , H.P. Schwarcz , Ultrastructure of Bone: hierarchical Features from Nanometer to Micrometer Scale Revealed in Focused Ion Beam Sections in the TEM, Calcified Tissue Int. 103 (2018) 606–616 .

[31] D.M. Binkley , J. Deering , H. Yuan , A. Gourrier , K. Grandfield , Ellipsoidal mesoscale mineralization pattern in human cortical bone revealed in 3D by plasma focused ion beam serial sectioning, J. Struct. Biol. (2020) 107615 .

[32] D.J. Buss , N. Reznikov , M.D. McKee , Crossfibrillar mineral tessellation in normal and Hyp mouse bone as revealed by 3D FIB-SEM microscopy, J. Struct. Biol. 212 (2020) 107603 .

[33] G.W. Bernard , D.C. Pease , An Electron Microscopic Study of Initial lntramembranous Osteogenesis, Am. J. Anat. 125 (1969) 271–290 .

[34] R.J. Midura , A. Vasanji , X. Su , A. Wang , S.B. Midura , J.P. Gorski , Calcospherulites isolated from the mineralization front of bone induce the mineralization of type I collagen, Bone 41 (2007) 1005–1016 .

[35] Z. Zou , T. Tang , E. Macías-Sánchez , S. Sviben , W.J. Landis , L. Bertinetti , P. Fratzl, Three-dimensional structural interrelations between cells, extracellular matrix, and mineral in normally mineralizing avian leg tendon, Proc. Natl Acad. Sci. 117 (2020) 14102–14109 .

[36] D.J. Buss , R. Kröger , M.D. McKee , N. Reznikov , Hierarchical organization of bone in three dimensions: a twist of twists, J. Struct. Biol. X (2021) 10 0 057 .

[37] M.D. McKee , D.J. Buss , N. Reznikov , Mineral tessellation in bone and the stenciling principle for extracellular matrix mineralization, J. Struct. Biol. 214 (2022) 107823 .

[38] F.A. Shah , K. Ruscsák , A. Palmquist , Transformation of bone mineral morphology: from discrete marquise-shaped motifs to a continuous interwoven mesh, Bone Rep 13 (2020) 100283 .

[39] Q. Wang , T. Tang , D. Cooper , F. Eltit , P. Fratzl , P. Guy , R. Wang , Globular structure of the hypermineralized tissue in human femoral neck, J. Struct. Biol. 212 (2020) 107606 .

[40] F.A. Shah , X. Wang , P. Thomsen , K. Grandfield , A. Palmquist , High-Resolution Visualization of the Osteocyte Lacuno-Canalicular Network Juxtaposed to the Surface of Nanotextured Titanium Implants in Human, Acs Biomater. Sci. Eng. 1 (2015) 305–313 .

[41] K. Grandfield , A. Palmquist , F. Ericson , J. Malmström , L. Emanuelsson , C. Slotte , E. Adolfsson , G.A. Botton , P. Thomsen , H. Engqvist , Bone response to freeform fabricated hydroxyapatite and zirconia scaffolds: a transmission electron microscopy study in the human maxilla, Clin. Implant Dent. R. 14 (2012) 461–469 .

[42] K. Grandfield , F. Ericson , B. Sandén , C.B. Johansson , S. Larsson , P. Thomsen , A . Palmquist , G.A . Botton , H. Engqvist , Ultrastructural characterisation of the hydroxyapatite-coated pedicle screw and human bone interface, Int. J. Nano Biomater. 4 (2012) 1 .

[43] P.H.S. Gomes-Ferreira, C. Micheletti, P. Buzo Frigério, F.R. de Souza Batista, N.G. Monteiro, O. Bim-júnior, P.N. Lisboa-Filho, K. Grandfield, Roberta Okamoto, PTH 1-34-functionalized bioactive glass improves periimplant bone repair in orchiectomized rats: Microscale and ultrastructural evaluation, Mater. Sci. Eng. C (2022) In press, doi: 10.1016/j.msec.2022.112688 .

[44] K. Grandfield , S. Gustafsson , A. Palmquist , Where bone meets implant: the characterization of nano-osseointegration, Nanoscale 5 (2013) 4302–4308 .

[45] O. Omar , T. Engstrand , L.K.B. Linder , J. ˚ Aberg , F.A. Shah , A. Palmquist , U. Birgersson , I. Elgali , M. Pujari-Palmer , H. Engqvist , P. Thomsen , In situ bone regeneration of large cranial defects using synthetic ceramic implants with a tailored composition and design, Proc. Natl. Acad. Sci. (2020) 202007635 .

[46] P. Ercius , O. Alaidi , M.J. Rames , G. Ren , Electron Tomography: a Three-Dimensional Analytic Tool for Hard and Soft Materials Research, Adv. Mater. 27 (2015) 5638–5663 .

[47] A. Palmquist , A multiscale analytical approach to evaluate osseointegration, J. Mater. Sci. Mater. Med. 29 (2018) 60 .

[48] P.A. Midgley , M. Weyland , 3D electron microscopy in the physical sciences: the development of Z-contrast and EFTEM tomography, Ultramicroscopy 96 (2003) 413–431 .

[49] M. Cantoni , L. Holzer , Advances in 3D focused ion beam tomography, MRS Bull. 39 (2014) 354–360 .

[50] M.D. Uchic , L. Holzer , B.J. Inkson , E.L. Principe , P. Munroe , Three-Dimensional Microstructural Characterization Using Focused Ion Beam Tomography, MRS Bull. 32 (2007) 408–416 .

[51] T.L. Burnett , R. Kelley , B. Winiarski , L. Contreras , M. Daly , A. Gholinia , M.G. Burke , P.J. Withers , Large volume serial section tomography by Xe Plasma FIB dual beam microscopy, Ultramicroscopy 161 (2016) 119–129 .

[52] D.C. Joy , Beam interactions, contrast and resolution in the SEM, J. Microsc.-Oxford 136 (1984) 241–258 .

[53] J. Goldstein , D.E. Newbury , D.C. Joy , C.E. Lyman , P. Echlin , E. Lifshin , L. Sawyer , J.R. Michael , Scanning Electron Microscopy and X-Ray Microanalysis, Springer US, New York NY, 2003 .

[54] R. Maria , Y. Ben-Zvi , K. Rechav , E. Klein , R. Shahar , S. Weiner , An unusual disordered alveolar bone material in the upper furcation region of minipig mandibles: a 3D hierarchical structural study, J. Struct. Biol. 206 (2019) 128–137 .

[55] E. Bonucci , Crystal ghosts and biological mineralization: fancy spectres in an old castle, or neglected structures worthy of belief? J. Bone Miner. Metab. 20 (2002) 249–265 .

[56] E. Bonucci , The locus of initial calcification in cartilage and bone, Clin. Orthop. Relat. Res. 78 (1971) 108–139 .

[57] M.D. McKee , A. Nanci , W.J. Landis , Y. Gotoh , L.C. Gerstenfeld , M.J. Glimcher , Effects of fixation and demineralization on the retention of bone phosphoprotein and other matrix components as evaluated by biochemical analyses and quantitative immunocytochemistry, J. Bone Miner. Res. 6 (1991) 937–945 .

[58] M.D. McKee , A. Nanci , Postembedding colloidal-gold immunocytochemistry of noncollagenous extracellular matrix proteins in mineralied tissues, Microsc. Res. Tech. 31 (1995) 44–62 .

[59] G. Mobus , B.J. Inkson , Nanoscale tomography in materials science, Mater. Today 10 (2007) 18–25 .

[60] A. Boyde , M.H. Hobdell , Scanning electron microscopy of primary membrane bone, Z. Zellforsch. 99 (1969) 98–108 .

[61] W.N. Addison , V. Nelea , F. Chicatun , Y.-.C. Chien , N. Tran-Khanh , M.D. Buschmann , S.N. Nazhat , M.T. Kaartinen , H. Vali , M.M. Tecklenburg , R.T. Franceschi , M.D. McKee , Extracellular matrix mineralization in murine MC3T3-E1 osteoblast cultures: an ultrastructural, compositional and comparative analysis with mouse bone, Bone 71 (2015) 244–256 .

[62] S. Boonrungsiman , E. Gentleman , R. Carzaniga , N.D. Evans , D.W. McComb , A.E. Porter , M.M. Stevens , The role of intracellular calcium phosphate in osteoblast-mediated bone apatite formation, Proc. Natl. Acad. Sci. 109 (2012) 14170–14175 .

[63] A. Boyde , J. Sela , Scanning electron microscope study of separated calcospherites from the matrices of different mineralizing systems, Calc. Tiss. Res. 26 (1978) 47–49 .

[64] J. Sela , I.A. Bab , Correlative transmission and scanning electron microscopy of the initial mineralization of healing alveolar bone in rats, Cells Tissues Organs 105 (1979) 401–408 .

[65] A. Ornoy , I. Atkin , J. Levy , Ultrastructural studies on the origin and structure of matrix vesicles in bone of young rats, Acta Anat. 106 (1980) 450–461 .

[66] J.E. Aaron , B. Oliver , N. Clarke , D.H. Carter , Calcified Microspheres as Biological Entities and Their Isolation from Bone, Histochem. J. 31 (1999) 455–470 .

[67] R.J. Midura , A. Vasanji , X. Su , S.B. Midura , J.P. Gorski , Isolation of Calcospherulites from the Mineralization Front of Bone, Cells Tissues Organs 189 (2008) 75–79 .

[68] L.J. Martino , V.L. Yeager , J.J. Taylor , An ultrastructural study of the role of calcification nodules in the mineralization of woven bone, Calcified Tissue Int. 27 (1979) 57–64 .

[69] J. Chen , M.A. Birch , S.J. Bull , Nanomechanical characterization of tissue engineered bone grown on titanium alloy in vitro, J. Mater. Sci. Mater. Med. 21 (2010) 277–282 .

[70] M. Ayoubi , A.F. van Tol , R. Weinkamer , P. Roschger , P.C. Brugger , A. Berzlanovich , L. Bertinetti , A. Roschger , P. Fratzl , Three-dimensional interrelationship between osteocyte network and forming mineral during human bone remodeling, Biorxiv (2020) 2020.11.20.391862 .

[71] L.A. Opperman , Cranial Sutures as Intramembranous Bone Growth Sites, Dev. Dyn. 219 (20 0 0) 472–485 .

[72] T. Miura , C.A. Perlyn , M. Kinboshi , N. Ogihara , M. Kobayashi-Miura , G.M. Morriss-Kay , K. Shiota , Mechanism of skull suture maintenance and interdigitation, J. Anat. 215 (2009) 642–655 .

[73] S. Weiner , W. Traub , Organization of hydroxyapatite crystals within collagen fibrils, FEBS Lett. 206 (1986) 262–266 .

[74] A.L. Arsenault , A comparative electron microscopic study of apatite crystals in collagen fibrils of rat bone, dentin and calcified turkey leg tendons, Bone Miner. 6 (1989) 165–177 .

[75] B. McEwen , M. Song , W. Landis , Quantitative determination of the mineral distribution in different collagen zones of calcifying tendon using high voltage electron microscopic tomography, J. Comput. Assist. Microsc. 3 (1990) 201–210 .

[76] W.J. Landis , M.J. Song , A. Leith , L. McEwen , B.F. McEwen , Mineral and organic matrix interaction in normally calcifying tendon visualized in 3D by HV EM tomography and graphic image reconstruction, J. Struct. Biol. 110 (1993) 39–54 .

[77] S. Lees , K.S. Prostak , V.K. Ingle , K. Kjoller , The loci of mineral in turkey leg tendon as seen by atomic force microscope and electron microscopy, Calcified Tissue Int. 55 (1994) 180–189 .

[78] R.M.V. Pidaparti , A. Chandran , Y. Takano , C.H. Turner , Bone mineral lies mainly outside collagen fibrils: predictions of a composite model for osteonal bone, J. Biomech. 29 (1996) 909–916 .

[79] E.A. McNally , H.P. Schwarcz , G.A. Botton , A.L. Arsenault , A Model for the Ultrastructure of Bone Based on Electron Microscopy of Ion-Milled Sections, PloS ONE 7 (2012) e29258 .

[80] E. McNally , F. Nan , G.A. Botton , H.P. Schwarcz , Scanning transmission electron microscopic tomography of cortical bone using Z-contrast imaging, Micron 49 (2013) 46–53 .

[81] H.P. Schwarcz , E.A. McNally , G.A. Botton , Dark-field transmission electron microscopy of cortical bone reveals details of extrafibrillar crystals, J. Struct. Biol. 188 (2014) 240–248 .

[82] N. Reznikov , J.A.M. Steele , P. Fratzl , M.M. Stevens , A materials science vision of extracellular matrix mineralization, Nat. Rev. Mater. 1 (2016) 16041 .

[83] Y. Liu , D. Luo , T. Wang , Hierarchical Structures of Bone and Bioinspired Bone Tissue Engineering, Small 12 (2016) 4611–4632 .

[84] F. Libonati , A.E. Vellwock , F. Ielmini , D. Abliz , G. Ziegmann , L. Vergani , Bone-inspired enhanced fracture toughness of de novo fiber reinforced composites, Sci. Rep.-Uk 9 (2019) 3142 .

[85] A .M. Torres , A .A . Trikanad , C.A . Aubin , F.M. Lambers , M. Luna , C.M. Rimnac , P. Zavattieri , C.J. Hernandez , Bone-inspired microarchitectures achieve enhanced fatigue life, Proc. Natl. Acad. Sci. 116 (2019) 24457–24462 .

[86] P. Fratzl , O. Kolednik , F.D. Fischer , M.N. Dean , The mechanics of tessellations – bioinspired strategies for fracture resistance, Chem. Soc. Rev. 45 (2015) 252–267 .

[87] B.J.F. Bruet , J. Song , M.C. Boyce , C. Ortiz , Materials design principles of ancient fish armour, Nat. Mater. 7 (2008) 748–756 .

[88] W. Yang , B. Gludovatz , E.A. Zimmermann , H.A. Bale , R.O. Ritchie , M.A. Meyers , Structure and fracture resistance of alligator gar (Atractosteus spatula) armored fish scales, Acta Biomater. 9 (2013) 5876–5889 .

[89] J.E. Moustakas-Verho , J. Cebra-Thomas , S.F. Gilbert , Patterning of the turtle shell, Curr. Opin. Genet. Dev. 45 (2017) 124–131 .

[90] B. Achrai , H.D. Wagner , The turtle carapace as an optimized multi-scale biological composite armor – a review, J. Mech. Behav. Biomed. 73 (2017) 50–67 .

[91] M.N. Dean , A.P. Summers , Mineralized cartilage in the skeleton of chondrichthyan fishes, Zoology 109 (2006) 164–168 .

[92] R. Seidel , M. Blumer , J. Chaumel , S. Amini , M.N. Dean , Endoskeletal mineralization in chimaera and a comparative guide to tessellated cartilage in chondrichthyan fishes (sharks, rays and chimaera), J. R. Soc. Interface 17 (2020) 20200474 .

[93] I.H. Chen , J.H. Kiang , V. Correa , M.I. Lopez , P.-.Y. Chen , J. McKittrick , M.A. Meyers , Armadillo armor: mechanical testing and micro-structural evaluation, J. Mech. Behav. Biomed. 4 (2011) 713–722 .

[94] A.P. Summers , Stiffening the stingray skeleton — An investigation of durophagy in Myliobatid stingrays (Chondrichthyes, Batoidea, Myliobatidae), J. Morphol. 243 (20 0 0) 113–126 .

[95] N. Reznikov , B. Hoac , D.J. Buss , W.N. Addison , N.M.T. Barros , M.D. McKee , Biological stenciling of mineralization in the skeleton: local enzymatic removal of inhibitors in the extracellular matrix, Bone 138 (2020) 115447 .

[96] H. Engqvist , G.A. Botton , M. Couillard , S. Mohammadi , J. Malmström , L. Emanuelsson , L. Hermansson , M.W. Phaneuf , P. Thomsen , A novel tool for high-resolution transmission electron microscopy of intact interfaces between bone and metallic implants, J. Biomed. Mater. Res. A 78A (2006) 20–24 .

[97] T. Jarmar , A. Palmquist , R. Brånemark , L. Hermansson , H. Engqvist , P. Thomsen , Technique for preparation and characterization in cross-section of oral titanium implant surfaces using focused ion beam and transmission electron microscopy, J. Biomed. Mater. Res. A 87A (2008) 1003–1009 .

[98] K. Grandfield , H. Engqvist , Focused Ion Beam in the Study of Biomaterials and Biological Matter, Adv. Mater. Sci. Eng. 2012 (2012) 1–6 .

[99] M.N. Dean , C.G. Mull , S.N. Gorb , A.P. Summers , Ontogeny of the tessellated skeleton: insight from the skeletal growth of the round stingray Urobatis halleri, J. Anat. 215 (2009) 227–239 .

[100] A.S. Posner , F. Betta , Synthetic amorphous calcium phosphate and its relation to bone mineral structure, Acc. Chem. Res. 8 (1975) 273–281 .